lubricants

MDPI

Article

Optimization Design of Aerostatic Bearings with Square Micro-Hole Arrayed Restrictor for the Improvement of Stability: Theoretical Predictions and Experimental Measurements

Puliang Yu [1,2,3,*], Jiong Lu [1,2,3], Qiang Luo [1,2,3], Guanghui Li [1,2,3] and Xianxiong Yin [1,2,3]

[1] The State Key Laboratory of Refractories and Metallurgy, School of Materials and Metallurgy, Wuhan University of Science and Technology, Wuhan 430081, China
[2] Key Laboratory of Metallurgical Equipment and Control Technology of Ministry of Education, School of Machinery and Automation, Wuhan University of Science and Technology, Wuhan 430081, China
[3] Hubei Key Laboratory of Mechanical Transmission and Manufacturing Engineering, School of Machinery and Automation, Wuhan University of Science and Technology, Wuhan 430081, China
* Correspondence: polo2008@wust.edu.cn

Abstract: Aerostatic bearings are widely used in ultra-precision manufacturing equipment as a crucial support component. However, turbulent vortices in the recess can induce micro-vibration of the aerostatic bearing, which can severely affect stability. To further suppress the formation of turbulent vortices and reduce the micro-vibration, an aerostatic bearing with a square micro-hole arrayed restrictor (SMAR) was designed and the influences of structural parameters of the SMAR on its static and dynamic performance were investigated using numerical simulations and experiments. The transient flow characteristics of aerostatic bearings with different numbers and spacing of micro-holes were studied using 3D large eddy simulation (LES), and the formation mechanism of turbulent vortices and the law of turbulent interaction between adjacent micro-holes were analyzed. The static performance and micro-vibration of the aerostatic bearing were measured experimentally to verify the effectiveness of the SMAR. The results show that the formation of turbulent vortices and micro-vibrations can be effectively reduced by the optimized design of the SMAR, while the static performance of the bearing is basically unchanged. The micro-vibration decreases rapidly with the number of micro-holes ranging from 1 to 36 and remains steady with the number of micro-holes ranging from 36 to 100. The micro-vibration decreases rapidly with the spacing of micro-holes ranging from 2 d_n to 8 d_n and remains steady with the spacing of micro-holes ranging from 8 d_n to 10 d_n. This study contributes to further understanding the mechanism of turbulent vortex formation in aerostatic bearings with a SMAR.

Keywords: square micro-hole arrayed restrictor; large eddy simulation; spacing of micro-holes; turbulent vortex; micro-vibration

Citation: Yu, P.; Lu, J.; Luo, Q.; Li, G.; Yin, X. Optimization Design of Aerostatic Bearings with Square Micro-Hole Arrayed Restrictor for the Improvement of Stability: Theoretical Predictions and Experimental Measurements. *Lubricants* **2022**, *10*, 295. https://doi.org/10.3390/lubricants10110295

Received: 30 September 2022
Accepted: 1 November 2022
Published: 4 November 2022

1. Introduction

Aerostatic bearings are widely used in semiconductor and precision equipment manufacturing because of their advantages, such as the near absence of friction, low heat generation, and high positioning accuracy [1–3]. Despite these advantages, the load capacity, stiffness, and stability of aerostatic bearings still need to be improved [4–6]. Chen et al. [7] found that recessed orifice restrictors can provide significantly higher load bearing capacity and stiffness compared to the inherent orifice restrictors. Zheng et al. [8] analyzed the transient pressure changes in the air film of aerostatic bearings by establishing a kinetic model and found that the recess has a significant effect on the load capacity of aerostatic bearings. Wen et al. [9] found that the structure of recess and uniform pressure tanks can significantly improve the static performance of aerostatic bearings. Zhou et al. [10] used pressure-sensitive film and image processing techniques to measure the air film pressure

distribution in aerostatic bearings with a recess. The theoretically calculated values were in general agreement with the experimental values.

However, although the recess structure can improve the pressure distribution in the air film and improve the static properties of the aerostatic bearing, it will also cause micro-vibration, or pneumatic hammer, which can reduce the stability or even damage the entire device [11]. Therefore, improving aerostatic bearing stability has become a hotspot in recent years of research. Yoshimura et al. [12] studied an aerostatic bearing with a T-shaped recess and found that pressure fluctuations caused micro-vibrations due to the unsteady airflow around the edge of bearings. Chen et al. [13] compared aerostatic bearings with and without recess and found that the instability of aerostatic bearings was related to the formation of vortices in the recess. Yifei et al. [14] studied the flow field of aerostatic bearings for numerical calculation and found that the vortex formed in the air film would affect the stability of aerostatic bearings. Zhu et al. [15] used the large eddy simulation method to simulate the airflow of aerostatic bearings with recess, and it was found that the vortex shedding phenomenon exists in the recess, and the pressure fluctuation caused by the turbulent vortex can cause micro-vibration of aerostatic bearings. Therefore, it can be concluded that the turbulent vortex formed in the recess is the main cause of the micro-vibration of the aerostatic bearing.

In order to improve the stability of aerostatic bearings, some researchers have also made related efforts to suppress the micro-vibration of the aerostatic bearing. Aoyama et al. [16], found that a rounded corner of the orifice outlet can suppress the formation of turbulent vortices near the orifice outlet and reduce the micro-vibration of the aerostatic bearing. Gao et al. [17], studied the effect of six different recess structures on the airflow characteristics and found that a conical recess with a certain curvature can suppress the formation of turbulent vortices in the recess. Chen et al. [18], proposed a novel restrictor structure with a micro-hole array and found that the structure can significantly inhibit the formation of turbulent vortices and thus reduce micro-vibrations through simulation calculations and experimental studies. Feng et al. [19], designed and fabricated four different orifice structures of aerostatic bearings using 3-D printing technology. The simulation and experimental results showed that the arc hole bearing can significantly improve the stability of the aerostatic bearing, and its static performance remains unchanged. In conclusion, the stability of aerostatic bearings with orifice restrictors can be improved by effectively suppressing the formation of turbulent vortices in the recess.

From the above references, aerostatic bearings with recesses have better static properties than those without recesses, but it is easier to induce turbulent vortex flow and micro-vibration. Although it has been found that the effect of vortices can be effectively reduced by controlling the operating parameters and changing the recess or orifice structures, it still does not meet the increasing accuracy requirements of ultra-precision motion platforms. Therefore, different structure optimization methods must be explored to further improve the stability of the aerostatic bearing.

In this paper, an aerostatic bearing with a square micro-hole arrayed restrictor (SMAR) is designed based on the analysis of the turbulent vortex formation mechanism. The flow characteristics can be modified to suppress the formation of turbulent vortices by optimizing the number and spacing of micro-holes. The theoretical load capacity, stiffness, and pressure fluctuations of the aerostatic bearing with the SMAR are obtained by the 3D LES. The effect of the number and spacing of micro-holes on the vortex structure and the micro-vibration of the aerostatic bearing has been clarified. Finally, the static and micro-vibration characteristics of the aerostatic bearing with the SMAR are verified by experiments.

2. Aerostatic Bearing with SMAR Design and Numerical Simulation Method

2.1. Design of Aerostatic Bearing with a SMAR

As shown in Figure 1, the main structure of the aerostatic bearing is a bearing pad, an orifice, a recess, and an air film. The airflow enters the recess through the orifice and then

spreads around to form a high-pressure air film. The high-pressure air film can support the bearing load [20–22]. The diameter of the aerostatic bearing is D = 80 mm, the diameter of the recess is D_q = 5 mm, the height of the recess is h_q = 0.1 mm, the height of the orifice is h_k = 0.3 mm, the diameter of the orifice is d_n, the thickness of air film is h_m = 15 μm, the inlet pressure is P_s = 0.5 MPa, and the outlet pressure is P_0 = 0.1 MPa.

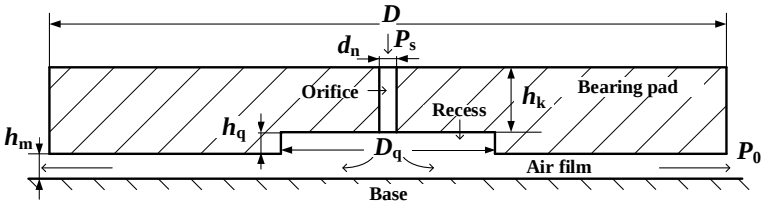

Figure 1. Structure of aerostatic bearing with a recess.

Figure 2 shows the vorticity cloud diagram, pressure cloud diagram, and streamlines for the aerostatic bearing with different orifice diameters by LES (orifice diameter is d_n = 0.28/0.2/0.12/0.04 mm). Figure 2a shows that a series of turbulent vortices are formed after the high-pressure air flows into the recess, and the turbulent complexity and vorticity decrease with decreasing orifice diameter. From the pressure distribution in Figure 2b, it can be seen that there is a low-pressure region at the center of the turbulent vortex, and the pressure distribution in the recess gradually decreases with decreasing orifice diameter. As seen in Figure 2b, the flow is deflected after entering the recess from the orifice, and the deflection angle decreases as the diameter of the orifice decreases.

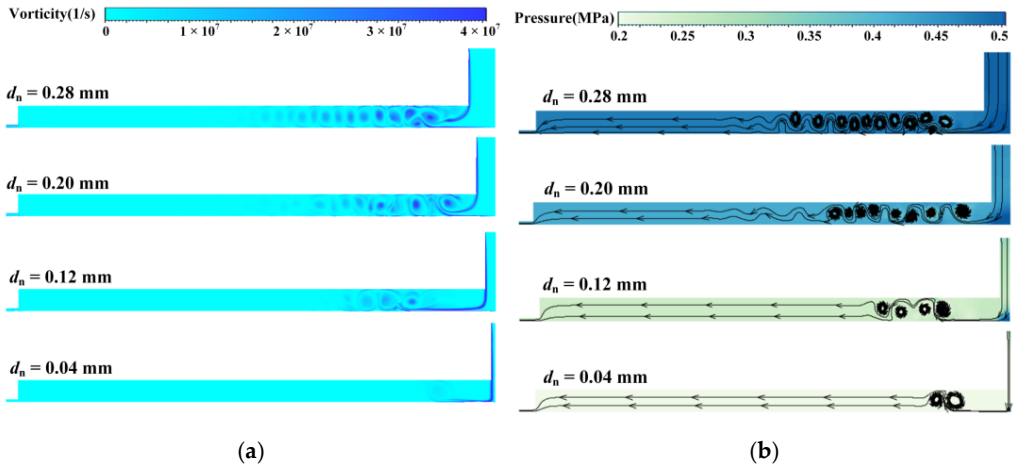

(**a**) (**b**)

Figure 2. (**a**) Vorticity cloud diagram; (**b**) Pressure cloud diagram and streamlines.

From the above analysis, it can be seen that reducing the orifice diameter suppresses the formation of turbulent vortices. It also reduces the pressure distribution in the recess, which leads to a decrease in the load capacity. If the orifice diameter can be reduced and the load capacity of the aerostatic bearing can be guaranteed, the flow field state of the aerostatic bearing can be improved, and its stability can be enhanced. Based on the above ideas, this paper designs an aerostatic bearing with a SMAR by keeping the total restriction area constant. The SMAR replaces the traditional single orifice with a square array of micro-holes (total restriction area is $S = 2\pi(d_n/2)^2$ mm^2) to increase the number of holes and reduce the diameter of individual holes. The structure of the aerostatic bearing with a SMAR is shown in Figure 3, and the structural and operating parameters are shown in Table 1.

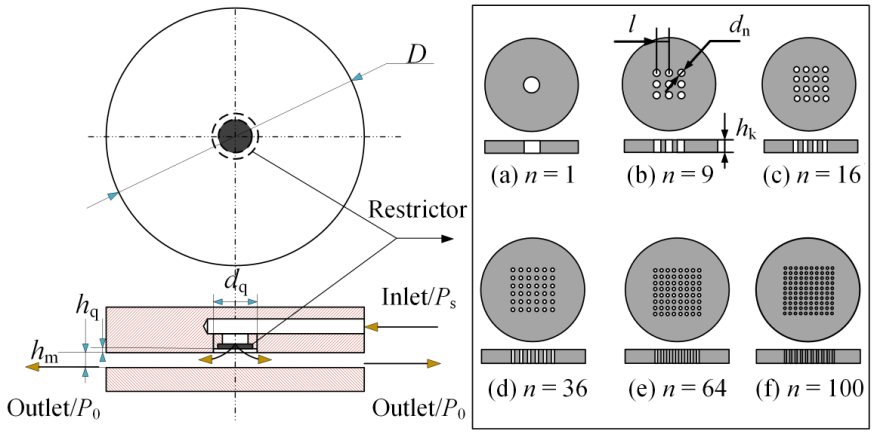

Figure 3. Structure of aerostatic bearing with (**a**) single-hole and (**b**–**f**) SMAR.

Table 1. Parameter variables of aerostatic bearing with a SMAR.

Parameter Variables	Value					
Number of micro-holes n	1	9	16	36	64	100
Orifice diameter d_n/mm	0.3	0.1	0.075	0.05	0.0375	0.03
spacing of micro-holes l/mm	0.1~1.0					
Inlet pressure P_s/MPa	0.5~0.6					
Air film thickness h_m/μm	5~30					
Outlet pressure P_0/MPa	0.1					

2.2. LES

The transient flow field characteristics of aerostatic bearings can be obtained by solving the full Navier–Stokes (N–S) equations. Li et al. [23,24], proposed a reconstruction discontinuous Galerkin method, which can solve the N–S equations more efficiently, accurately, and robustly. Kabir et al. [25,26]. found that the Bézier method can better solve the initial value and boundary value problems. Reynolds Averaged Navier–Stokes (RANS) simulation method can be used to study turbulence, but it cannot accurately analyze the instantaneous details of turbulence [15,18]. Direct numerical simulation (DNS) can directly solve N–S equations without turbulence models, which can obtain accurate results in theory, but the calculation scale is huge. Large eddy simulation (LES) can directly calculate large-scale turbulent vortices and simulate small-scale turbulent vortices. The accuracy and computational cost of LES are between RANS and DNS, and it is widely used in the simulation of the transient flow field of aerostatic bearings [15,27].

The control equations of the large eddy simulation (LES) model are the time-dependent Favre Filtered Navier–Stokes equations [27], including the momentum equation and the continuity equation:

$$\frac{\partial \overline{\rho}}{\partial t} + \frac{\partial}{\partial x_i}(\overline{\rho}\widetilde{u_i}) = 0 \tag{1}$$

$$\frac{\partial}{\partial t}(\overline{\rho}\widetilde{u_i}) + \frac{\partial}{\partial x_j}(\overline{\rho}\widetilde{u_i}\widetilde{u_j}) = -\frac{\partial \overline{P}}{\partial x_i} + \frac{\partial \widetilde{\sigma_{ij}}}{\partial x_j} - \frac{\partial}{\partial x_j}(\widetilde{\tau_{ij}}) \tag{2}$$

where: density ρ and pressure P are spatially filtered (denoted by "$^-$"), velocity u_i and u_j are density–weighted using Favre filter (denoted by "$\tilde{}$"). is the viscous stress tensor, which can be defined as:

$$\widetilde{\sigma_{ij}} = \mu\left(\frac{\partial \widetilde{u_i}}{\partial x_j} + \frac{\partial \widetilde{u_j}}{\partial x_j} - \frac{2}{3}\delta_{ij}\frac{\partial \widetilde{u_k}}{\partial x_k}\right) \tag{3}$$

τ_{ij} is the subgrid-scale (SGS) stress, which cannot be derived by direct calculation of the differential equations, so the vortex viscosity concept is assumed, as shown in Equation (4):

$$\tau_{ij} = 2\mu_{SGS}\overline{S_{ij}} - \frac{1}{3}\tau_{kk}\delta_{ij} \tag{4}$$

$$\overline{S_{ij}} = \frac{1}{2}\left(\frac{\partial \overline{u_i}}{\partial x_j} + \frac{\partial \overline{u_j}}{\partial x_i}\right) \tag{5}$$

This paper uses the WALE model for the SGS, which can better resolve the near-wall turbulence and more accurately characterize the zero turbulent viscosity of the laminar shear flow [28,29].

2.3. Computational Mesh and Solution Set

Due to the symmetry of the aerostatic bearing structure, a 1/4 air domain model is established in the simulation process to improve computational efficiency. A hexahedral structured mesh is used for numerical calculations, and the mesh is shown in Figure 4a. In order to enhance the resolution accuracy of turbulent vortices in the near-wall region of the flow field, refinement is performed at the recess. The resolution scale of the near-wall mesh is characterized by the value of y^+, which is no more than 1 [15]. The y^+ is defined as $y^+ = \sqrt{\rho\tau_w}y/\mu$, where y is the distance from the center of the first layer of the near-wall mesh to the boundary. The τ_w is the wall shear stress. The conclusion of grid independence is obtained by comparing the load capacity fluctuation and its standard deviation in the simulation results (as described in Section 3.2), as shown in Table 2. It turns out that the mesh before and after refinement has little effect on the numerical simulation results. Therefore, the subsequent numerical simulation results in this paper can be considered to be grid independent.

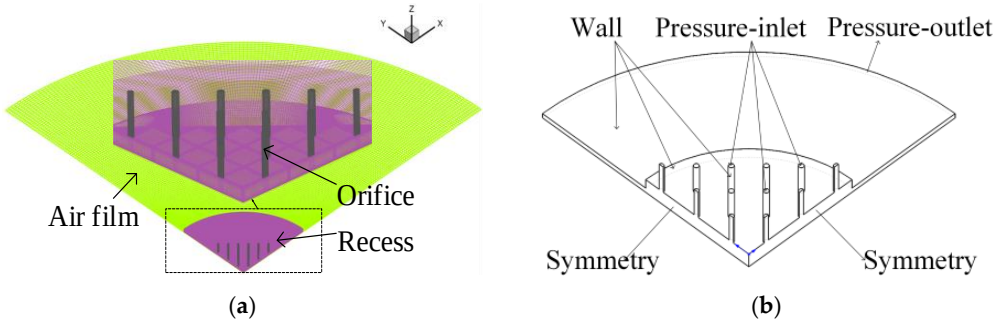

Figure 4. (**a**) Computational grid; (**b**) Boundary conditions.

Table 2. Grid independence verification parameter (where δ denotes mesh scale (μm^3)).

Mesh	Recess		Orifice		Air film		y^+_{max}	Total Number	Fluctuations of Load Capacity F(N)	Standard Deviation σ
	δ_{min}	δ_{max}	δ_{min}	δ_{max}	δ_{min}	δ_{max}				
Coarse	1.26	1590	30.25	103.15	1267	9825	1.6	2084581	0.38	0.049
Fine	0.58	632					0.7	3423926	0.39	0.051

Figure 4b shows the boundary conditions of the aerostatic bearing, the inlet pressure is Ps, and the outlet pressure P_0 is set as the ambient pressure. The left and right sections of the model are set as symmetric, and the rest of the boundaries are set as a wall. The gas inside the aerostatic bearing is assumed to be the ideal air.

To enhance the computational efficiency and ensure sufficient computational accuracy, the PISO (Pressure-Implicit with Splitting of Operators) algorithm is chosen for the pressure–velocity interaction algorithm in the paper, and the second-order windward interpolation is chosen for the density and turbulent kinetic energy. The time step is obtained by the CFL (Courant–Friedrichs–Lewy) condition, and the CFL condition is shown in the equation [30]:

$$u\Delta t/\Delta x < 1 \tag{6}$$

where: u is the characteristic velocity within the flow field, Δt is the time step, and Δx is the flow field grid characteristic scale.

The instantaneous load capacity F of the aerostatic bearing can be obtained by integrating the pressure distribution on the air film surface as follows:

$$F = \int_0^R \int_0^{2\pi} (p - p_0) r dr d\theta \tag{7}$$

The standard deviation of the fluctuation of the instantaneous load capacity is used to describe the magnitude of micro-vibration of the aerostatic bearing, as shown in Equation (8):

$$\sigma = \sqrt{\frac{\sum_{i=1}^{m} (F_i - \overline{F})}{m}} \tag{8}$$

where: F_i represents the time-varying load capacity of the ith time step. $\overline{F}$ represents the average load capacity which is the average value of instantaneous load capacity. m represents the number of iteration steps. $F_i - \overline{F}$ represents the load capacity fluctuation.

The stiffness is the derivative of the average bearing capacity for the amount of change in the height of the air film, as shown in Equation (9):

$$K = \frac{d\overline{F}}{dh} \tag{9}$$

3. Results and Discussion

3.1. Turbulent Vortex Formation Mechanism

To illustrate the formation mechanism of turbulent vortices in the recess (as described in Section 2.1), the airflow inside the recess is simplified, as shown in Figure 5. After the high-pressure airflow V_1 enters the recess, it separates from the upper wall because of the sudden expansion of the orifice outlet and forms the separation region A. The airflow V_1 vertically reaches the lower wall, forming compression region B. The airflow channel C is formed between the separation region A and the compression region B. The airflow V_1 flows into the recess through channel C and changes to airflow V_2 with the deflect angle α. The airflow V_2 changes to V_3 after impacting the lower wall. Subsequently, V_3 impacts the upper wall, causing velocity separation and forming airflow V_4 and V_5. These airflows with different directions and velocities interact with the surrounding air and form a series of turbulent vortices of different scales. Moreover, turbulent vortices experience formation, development, shedding, and dissipation in the recess, which affects the stability of the aerostatic bearing.

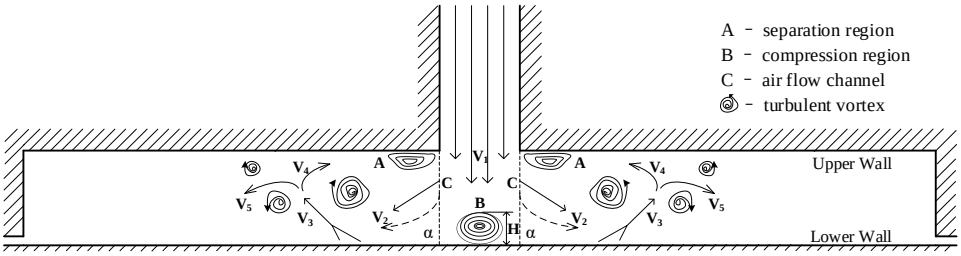

Figure 5. Aerostatic bearings airflow diagram.

3.2. Effect of the Different Numbers of Micro-Holes on Micro-Vibration Characteristics

To investigate the effect of different numbers of micro-holes on the static and micro-vibrational properties of the aerostatic bearing, the simulation analysis of the aerostatic bearing was carried out based on keeping the spacing of micro-holes constant.

Figure 6 shows the average load capacity and stiffness of the aerostatic bearing for different numbers of micro-holes. As can be seen from Figure 6, the load capacity and

stiffness of aerostatic bearings with different numbers of micro-holes are basically the same. Thus, changing the number of micro-holes does not affect the static performance of the aerostatic bearing.

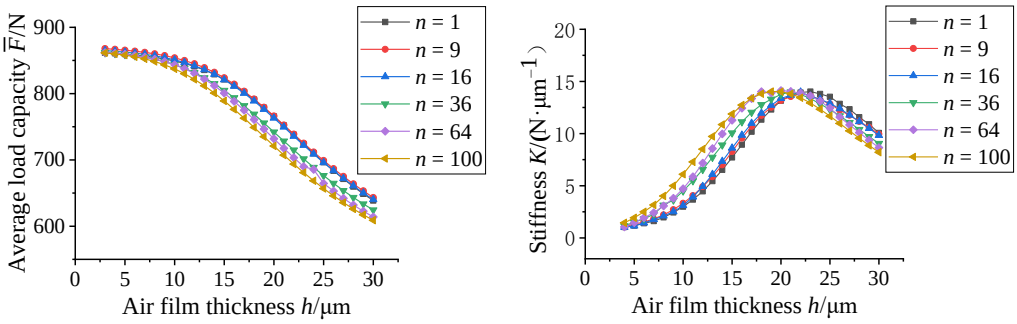

(**a**) (**b**)

Figure 6. The static performance of aerostatic bearings with different number of micro-holes: (**a**) Average load capacity curves; (**b**) Stiffness variation curves.

Figure 7 shows the pressure cloud diagram, streamlines, and velocity cloud diagram on the symmetry surface of aerostatic bearings with different micro-hole numbers. It can be seen that the aerostatic bearing with a single-hole restrictor has the largest turbulent vorticity, the deflection angle α of the airflow V_2, and compression region B in the recess compared to the aerostatic bearing with the SMAR. Among the aerostatic bearings with the SMAR, the deflection angle α, the complexity of the turbulent vortices, and the region B in the recesses decrease significantly as the number of micro-holes increases, but the velocity of the airflow V_1 in the orifice increases.

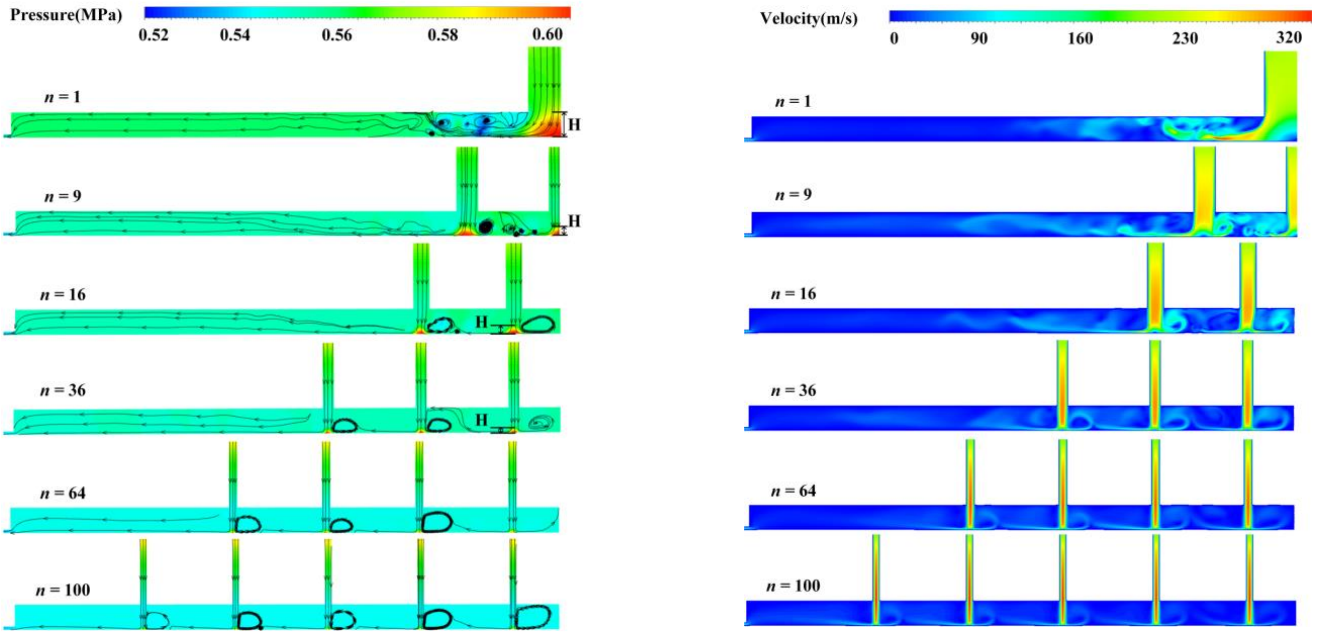

(**a**) (**b**)

Figure 7. 2D flow structures in the recess of aerostatic bearing with different number of micro-holes: (**a**) Pressure cloud diagram and streamlines; (**b**) Velocity cloud diagram.

In addition, more turbulent vortices are generated between the micro-holes than outside due to the interaction of different airflows V_2 between neighboring micro-holes. However, as the number of micro-holes increases, the interaction effect will gradually

weaken or even disappear. This is because the velocity and deflection angle α of airflow V_2 decrease as the number of micro-holes increases. Therefore, the airflow outside the array holes is more likely to interact with the surrounding air and gradually dissipate. The interaction of different airflows V_2 from adjacent holes is gradually weakened.

In order to capture the transient turbulent flow details of the airflow among adjacent micro-holes, the flow field variation of the aerostatic bearing is analyzed by 3-D LES. Figure 8 shows the iso-surfaces of vorticity of the aerostatic bearing with the different numbers of micro-holes. As can be seen from Figure 8, compared with the aerostatic bearing with a SMAR, more high vorticity vortexes are formed near the orifice of the aerostatic bearing with a single hole. In the aerostatic bearing with a SMAR, the vorticity and complexity of turbulent vortices in the recess gradually decrease with the increase in micro-holes. Moreover, the interaction of turbulent vortices among the adjacent micro-holes also gradually decreases, and the vortex structure tends to be orderly and stable. Compared with 2D, the 3D flow field can more clearly observe the airflow interaction among all adjacent micro-holes and the details of vortex structure changes which helps analyze the mechanism of micro-vibration suppression.

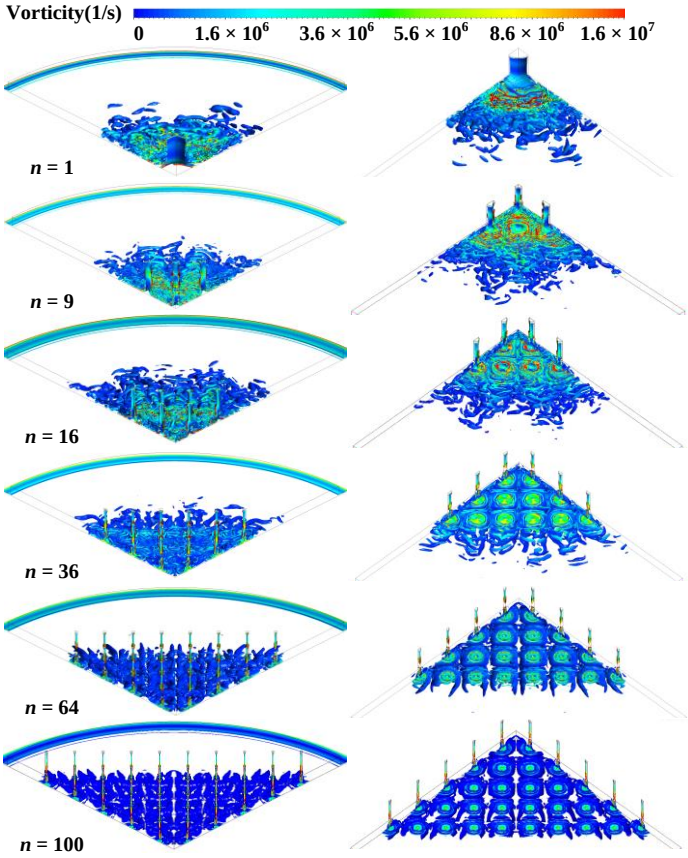

Figure 8. Iso-surfaces of vorticity in the recess of aerostatic bearing with different number of micro-holes.

To quantitatively analyze the suppressing effect of the SMAR on turbulent vortices, the variation of the load capacity fluctuation of aerostatic bearings with time is shown in Figure 9. It can be seen that with the increase in the number of micro-holes, the amplitude of load capacity fluctuation decreases. The corresponding standard deviation is shown in Figure 10. It can be seen that the standard deviation of the load capacity fluctuation will decline rapidly with the number of micro-holes from 1 to 36 and remains stable from 36 to 100. It can be concluded that increasing the number of micro-holes can suppress the micro-vibration of the aerostatic bearing and improves its stability.

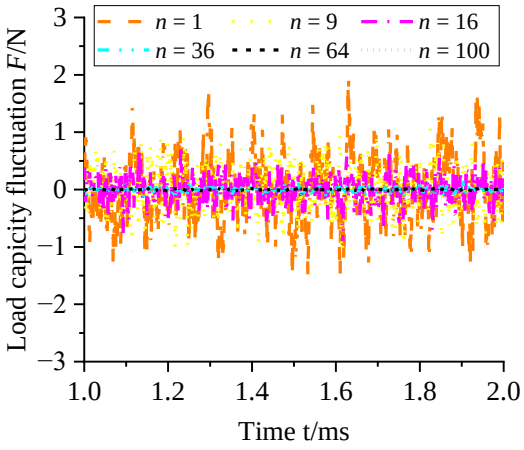

Figure 9. Fluctuations of load capacity of aerostatic bearing with different number of micro-holes.

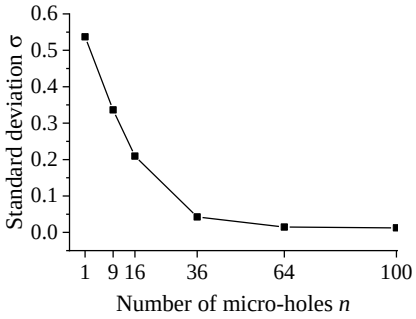

Figure 10. The standard deviation of load capacity fluctuation of aerostatic bearing with different number of micro-holes.

3.3. Effect of the Spacing of Micro-Holes Variation on Micro-Vibration Characteristics

In this section, the effect of a change in the spacing of micro-holes on the static and micro-vibration characteristics of the aerostatic bearing is studied.

Figure 11 shows the average load capacity and stiffness of the aerostatic bearing (the number of micro-holes is n = 36) with different spacing of micro-holes. It can be seen that the average load capacity and stiffness of the aerostatic bearing with different spacing of micro-holes are consistent, which indicates that changing the spacing of micro-holes basically does not affect the static performance of the aerostatic bearing.

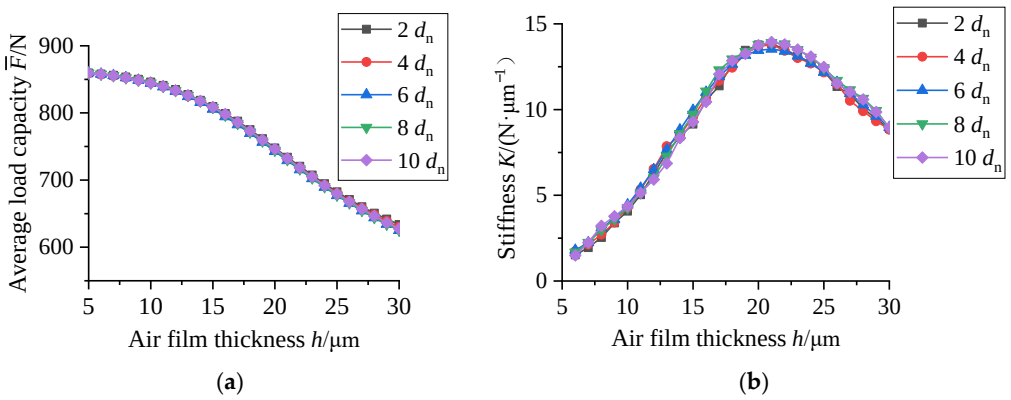

Figure 11. The static performance of aerostatic bearings with different spacing of micro-holes: (**a**) Average load capacity curves; (**b**) Stiffness variation curves.

Figure 12 shows the pressure cloud diagram, streamlines, and velocity cloud diagram of the symmetry surface of the aerostatic bearing (number of micro-holes is n = 36) with different spacing of micro-holes. It can be seen that the pressure distribution in the recess is almost unaffected by the variation of the micro-hole spacing. However, as the spacing of micro-holes increases, the effect of the airflow interaction between adjacent micro-holes becomes weaker. This is because the change of the micro-hole spacing has almost no effect on the velocity and deflection angle α of airflow V_2. The smaller the hole spacing is, the stronger the interaction between airflow V_2 from adjacent holes will be. With the increase in the spacing of micro-holes, airflow V_2 interacts more with the surrounding air and dissipates gradually, avoiding direct interaction with different airflows V_2 from adjacent holes, so the airflow field becomes more stable.

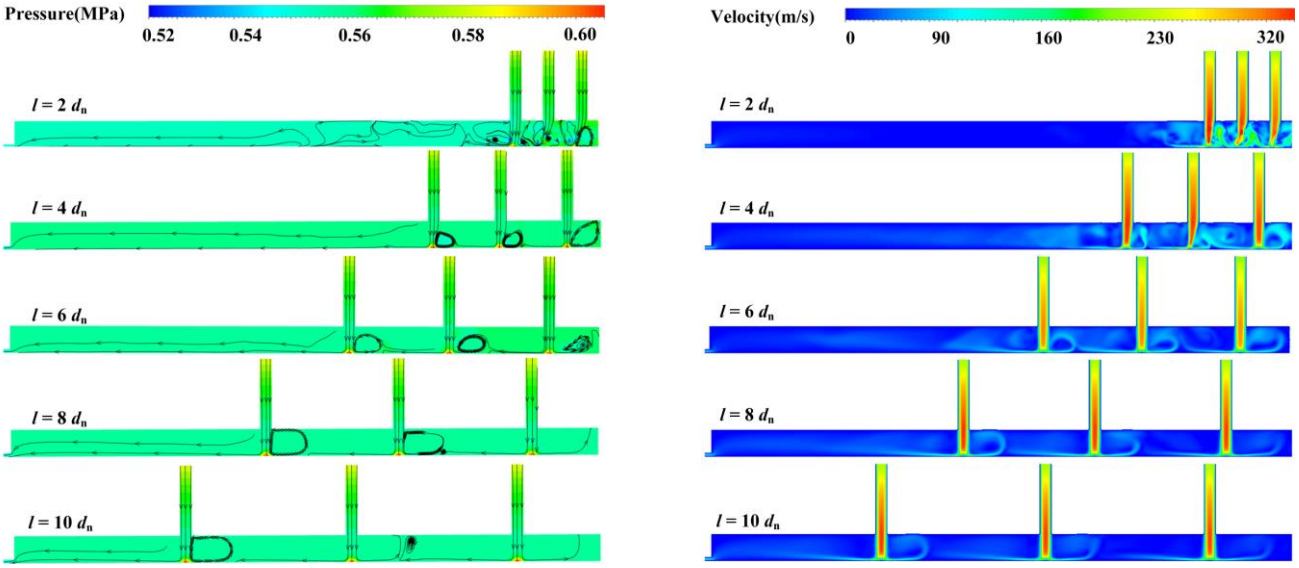

(**a**) (**b**)

Figure 12. 2D flow structures in the recess of aerostatic bearing with different spacing of micro-holes: (**a**) Pressure cloud diagram and streamlines; (**b**) Velocity cloud diagram.

Figure 13 shows the iso-surfaces of vorticity of the aerostatic bearing (the number of micro-holes is n = 36) with different spacing of micro-holes. In the 3D flow field, the details of the airflow interactions between all adjacent holes can be easily captured. As can be seen from Figure 13, as the spacing of micro-holes increases, the complexity and vorticity of turbulent vortices gradually decrease, especially among adjacent orifices. The vortex structure in the recess also develops in the direction of order and stability.

Figure 14 shows the variation curve of the load capacity of aerostatic bearings (number of micro-holes is n = 9/36/64) with time. It can be seen that with the increase in spacing of micro-holes, the amplitude of load capacity fluctuation of three types of aerostatic bearings decreases. Figure 15 shows the corresponding standard deviation. It can be seen that the standard deviation of load capacity fluctuation will decline quickly during the micro-hole spacing from 2 d_n to 8 d_n and remains stable during the spacing from 8 d_n to 10 d_n. It can be concluded that increasing the spacing of micro-holes can suppress the micro-vibration of the aerostatic bearing.

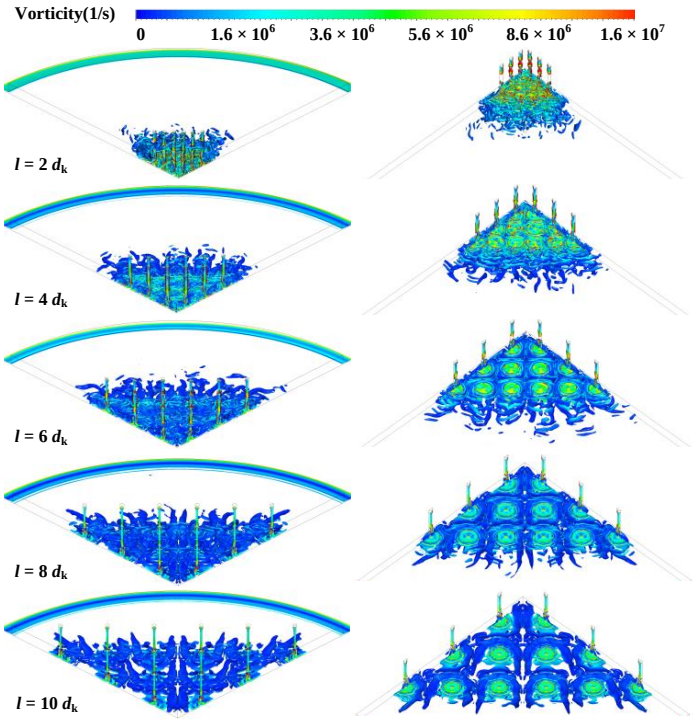

Figure 13. Iso-surfaces of vorticity in the recess of aerostatic bearing with different spacing of micro-holes.

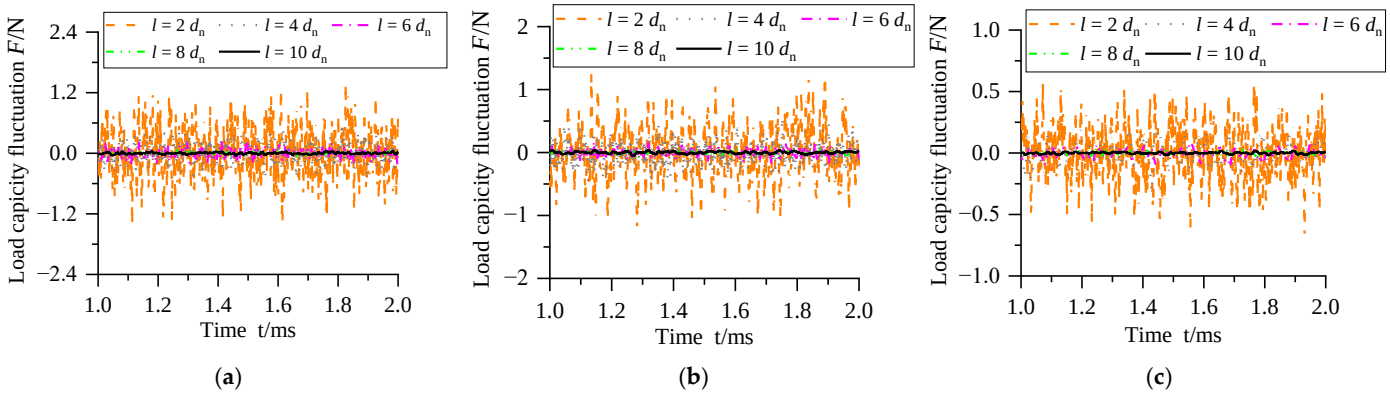

Figure 14. (**a**–**c**) Fluctuations of load capacity (number of micro-holes is $n = 9/36/64$).

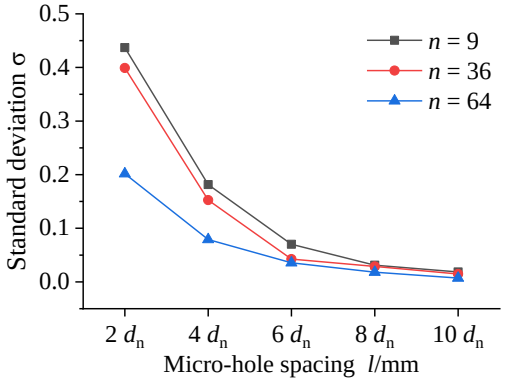

Figure 15. The standard deviation of load capacity fluctuation of aerostatic bearing with different spacing of micro-holes.

4. Experimental Research

Several aerostatic bearings with a SMAR were produced to verify the validity of the LES method and results. In addition, the static and dynamic performance of aerostatic bearings were tested. The influence of the number and spacing of micro-holes on load capacity and micro-vibration characteristics of the aerostatic bearing with a SMAR was verified by experiments.

4.1. Manufacturing the Aerostatic Bearing with a SMAR

The photo of aerostatic bearings with n = 1 single-hole, n = 9 SMAR (l = 3 d_n), and n = 36 SMAR (l = 4/6/8 d_n) are shown in Figure 16. Details of the SMAR are captured by electron microscope. The aerostatic bearing consists of two parts, the restrictor, and the bearing pad. The bearing pad is made of aluminum alloy. The single-hole restrictor is made of a cylindrical ruby, processed by laser drilling, and then assembled into the recess of the bearing pad. The micro-hole diameter of the SMAR designed in this study can reach the micron-level, while the picosecond laser drilling technology can achieve micron-level accuracy and can ensure a more uniform micro-hole size. Therefore, the SMAR is made of cylindrical aluminum alloy by using a picosecond laser processing technology and then installed in the recess on the bearing pad.

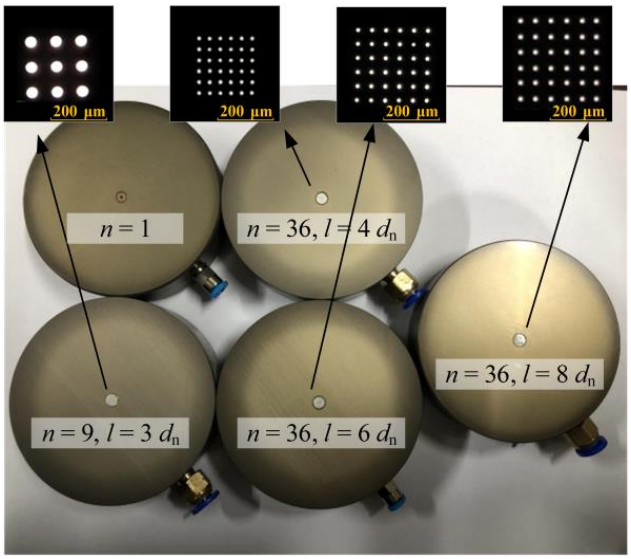

Figure 16. Photo of aerostatic bearings with single-hole and different SMARs.

4.2. Load Capacity Testing

Figure 17 shows the experimental platform of load capacity testing. The experimental platform consists of a cylinder, a force transducer (PBCL, range 200–700 kg, Zhongjing, Shanghai, China), an inductance micrometer (TESA-TT20-GTL22, range ±2 mm, resolution 0.1 μm, TESA, Switzerland), two aerostatic bearings with a SMAR (n = 9, l = 3 d_n, and n = 36, l = 6 d_n), and a marble platform. The thickness of the air film is changed by adjusting the cylinder pressure and measured by the inductance micrometer mounted on the marble. The load capacity of the aerostatic bearing is measured by the force transducer. After multiple measurements, the average value was taken.

Figure 18 compares the experimental and simulation results of the load capacity of the aerostatic bearing with different numbers of micro-holes. The experimental results are in good agreement with the simulation results, and the maximum error is less than 5%.

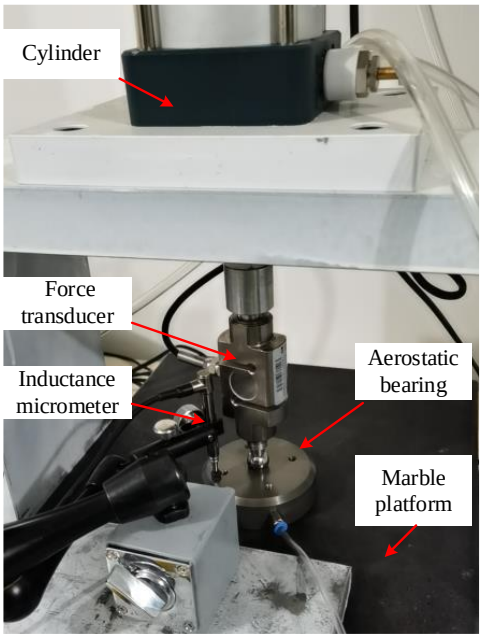

Figure 17. Static performance test platform.

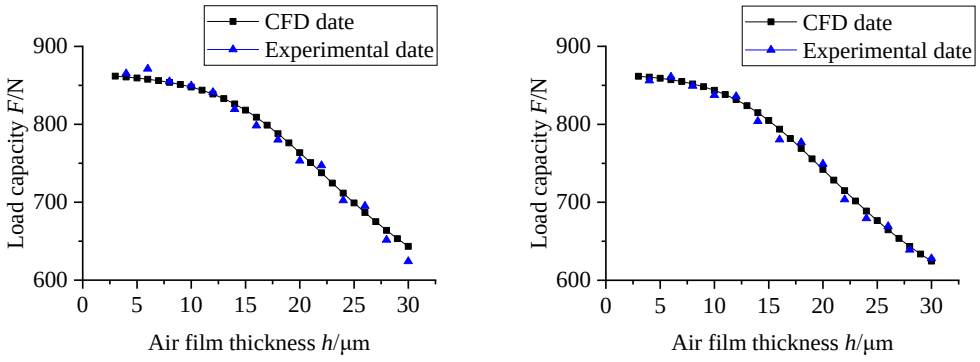

Figure 18. Comparison of experimental and simulation results of load capacity. (**a**) number of micro-holes is $n = 9$, $l = 3\ d_n$; (**b**) number of micro-holes is $n = 36$, $l = 6\ d_n$.

4.3. Micro-Vibration Testing

Figure 19 shows the experimental platform for micro-vibration testing. The experimental platform consists of aerostatic bearings ($n = 1$ single-hole, $n = 9$ SMAR ($l = 3\ d_n$), and $n = 36$ SMAR ($l = 4/6/8 d_n$)), weights, a laser displacement sensor (LK-G500, reproducibility 2 μm, KEYENCE, Japan), an accelerometer (ULT-2015, sensitivity 2500 mV/g, resolution 0.000004 g, QUATR, Beijing, China), a marble platform, a vibration isolation platform, a data acquisition card (NI-9234, 24-bit, America), and a PC (Lenovo, China) terminal. The thickness of the air film is changed by adjusting the weights and measured by the laser displacement sensor. The vibration acceleration of the aerostatic bearing is obtained by the accelerometer. The vibration signal is dealt with by a PC terminal.

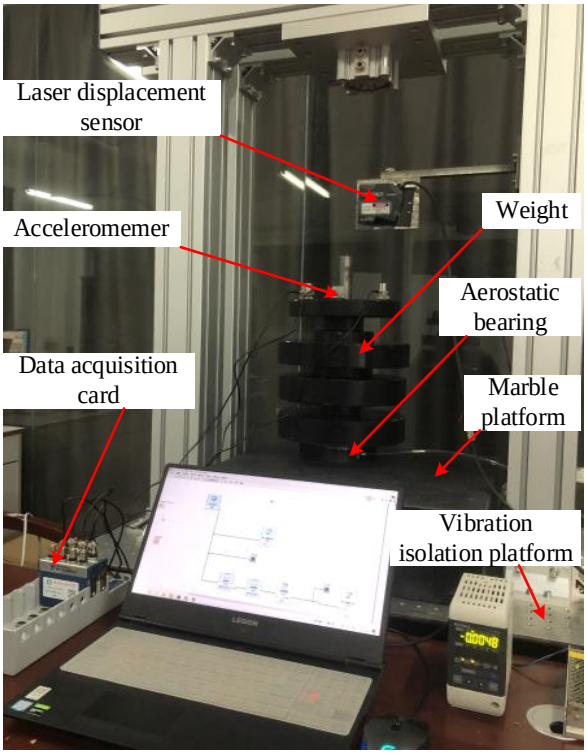

Figure 19. Micro-vibration test platform.

Figure 20a shows vibration accelerations in the time domain for bearings (thickness is h_m = 30 μm, inlet pressure is P_s = 0.6 MPa) with the different numbers of micro-holes. As can be seen from Figure 20a, the vibration acceleration amplitude of the aerostatic bearing with a single hole is the largest and the smallest at the aerostatic bearing with n = 36. Figure 20b shows vibration accelerations in the time domain for bearings (thickness is h_m = 30 μm, inlet pressure is P_s = 0.6 MPa) with different spacing of micro-holes. As can be seen from Figure 20b, the vibration acceleration amplitude of the aerostatic bearing is the largest at $l = 4d_n$, followed by that at $l = 6d_n$, and the smallest at $l = 8d_n$.

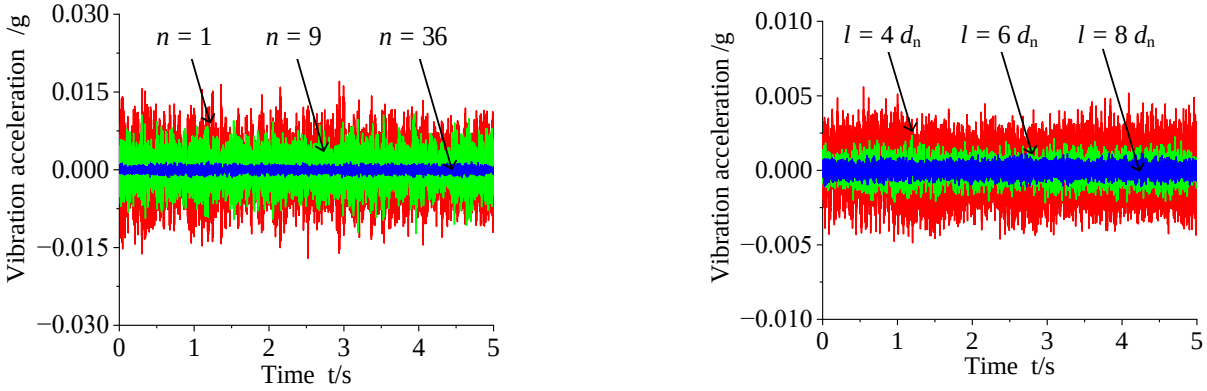

Figure 20. (**a**) Vibration accelerations in the time domain for the bearings with different numbers of micro-holes; (**b**) Vibration accelerations in the time domain for the bearings· (number of micro-holes is n = 36) with different spacing of micro-holes.

As shown in Figure 21, vibration acceleration in the frequency domain is FFT transformed from the above time domain signal. From Figure 21a (thickness is h_m = 30 μm, inlet pressure is P_s = 0.6 MPa), it can be concluded that the peak amplitude gradually decreases

with the increase in the number of micro-holes. From Figure 21b (thickness is h_m = 30 μm, inlet pressure is P_s = 0.6 MPa), it can be concluded that the peak amplitude gradually decreases with the increase in the spacing of micro-holes. The above experimental results prove that the SMAR can effectively suppress the micro-vibration and significantly improve the stability of the aerostatic bearing.

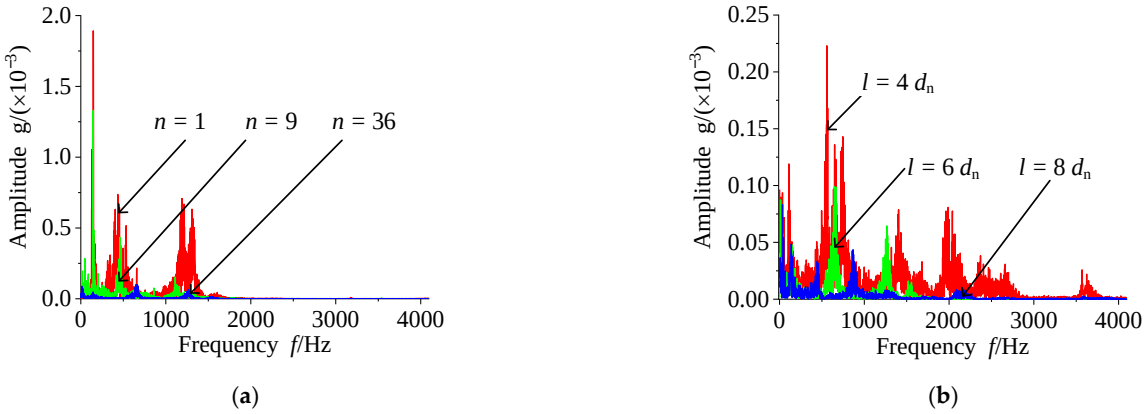

Figure 21. (**a**) Frequency characteristics of vibration accelerations for the bearings with different micro-holes; (**b**) Frequency characteristics of vibration accelerations for the bearings (number of micro-holes is n = 36) with different spacing of micro-holes.

5. Conclusions

In this paper, an aerostatic bearing with a SMAR was designed to suppress turbulent vortices and reduce micro-vibration, and the effects of different structural parameters on its static and dynamic characteristics were investigated numerically and experimentally. The transient flow characteristics of the aerostatic bearing with single-hole restrictor and the SMAR were investigated. The LES method is used to resolve the details of transient 3D turbulence, and the formation mechanism of turbulent vortices and the law of turbulent interaction between adjacent micro-holes were analyzed. The accuracy of the simulation model and the effectiveness of the SMAR is verified by load capacity testing and micro-vibration testing. According to the results in this paper, the following conclusions can be drawn:

(1) The aerostatic bearing with the SMAR can effectively reduce the micro-vibration characteristics by optimizing the structural parameters, while the load capacity and stiffness basically keep constant when the SMAR keeps essentially the same total restriction area.

(2) Increasing the number of micro-holes can suppress the formation of turbulent vortices near the orifice by reducing the deflection angle α of the airflow and the range of the compression region B. When the number of micro-holes is less than 36, the micro-vibration of the aerostatic bearing decrease remarkably with the increase in the number of micro-holes. When the number of micro-holes is more than 36, the micro-vibration of the aerostatic bearing decreases insignificantly with the increase in the number of micro-holes. However, the micro-hole number should be carefully chosen in optimization design, because of manufacturing cost and possible blockage of the micro-hole.

(3) Increasing the spacing of micro-holes can inhibit the formation of turbulent vortices among the adjacent micro-holes by reducing the interaction of the different airflows from different micro-holes. When the spacing of micro-holes is less than $8d_n$, the micro-vibration of the aerostatic bearing decreases remarkably with the increase in the spacing of micro-holes. When the spacing of micro-holes is more than $8d_n$, the micro-vibration of the aerostatic bearing decrease insignificantly with the increase in the spacing of micro-holes. In the optimization design, the larger spacing of micro-holes in the restrictor should be selected to ensure a better micro-vibration suppression effect.

This study provides a valuable reference for further reducing the micro-vibration of aerostatic bearings and is helpful to further study the formation and interaction mechanism of turbulent vortices in the aerostatic bearing. The limitation of this study is that the internal airflow field characteristics of the aerostatic bearing in the recess have not been observed by experiments such as particle image velocimetry (PIV), which is also the direction of our future work.

Author Contributions: Conceptualization, P.Y. and J.L.; methodology, G.L.; software, X.Y. and Q.L.; validation, P.Y. and J.L.; Writing review and editing, P.Y. and J.L. All authors have read and agreed to the published version of the manuscript.

Funding: This research was funded by the National Natural Science Foundation of China, grant number 51705378; Youth Fund Project for The State Key Laboratory of Refractories and Metallurgy, grant number 2018QN15, and Hubei Natural Science Foundation, grant number 2018CFB757.

Data Availability Statement: Not applicable.

Acknowledgments: Numerical calculation was supported by the High-Performance Computing Center of Wuhan University of Science and Technology.

Conflicts of Interest: The authors have no competing interests to declare that are relevant to the content of this article.

References

1. Maamari, N.; Krebs, A.; Weikert, S.; Wild, H.; Wegener, K. Stability and dynamics of an orifice based aerostatic bearing with a compliant back plate. *Tribol. Int.* **2019**, *138*, 279–296. [CrossRef]
2. Lu, Z.W.; Zhang, J.A.; Liu, B.; Huang, J. Study on the Gas Film Flow Field and its Influencing Factors at the Outlet of the Orifice of the Aerostatic Bearing. *Shock Vib.* **2020**, *2020*, 1–16. [CrossRef]
3. Li, W.J.; Wang, G.Q.; Feng, K.; Zhang, Y.C.; Wang, P. CFD-based investigation and experimental study on the performances of novel back-flow channel aerostatic bearings. *Tribol. Int.* **2022**, *165*, 107319. [CrossRef]
4. Otsu, Y.; Somaya, K.; Yoshimoto, S. High-speed stability of a rigid rotor supported by aerostatic journal bearings with compound restrictors. *Tribol. Int.* **2011**, *44*, 9–17. [CrossRef]
5. Gao, Q.; Chen, W.Q.; Lu, L.H.; Huo, D.H.; Cheng, K. Aerostatic bearings design and analysis with the application to precision engineering: State-of-the-art and future perspectives. *Tribol. Int.* **2019**, *135*, 1–17. [CrossRef]
6. Liu, Z.F.; Wang, Y.M.; Cai, L.G.; Zhao, Y.S.; Cheng, Q.; Dong, X.M. A review of hydrostatic bearing system: Researches and applications. *Adv. Mech. Eng.* **2017**, *9*, 1–27. [CrossRef]
7. Chen, Y.S.; Chiu, C.C.; Cheng, Y.D. Influences of operational conditions and geometric parameters on the stiffness of aerostatic journal bearings. *Precis. Eng.* **2010**, *34*, 722–734. [CrossRef]
8. Zheng, Y.Q.; Yang, G.W.; Cui, H.L.; Hou, Y. Pneumatic stability analysis of single-pad aerostatic thrust bearing with pocketed orifice. *P. I. Mech. Eng. J-J. Eng.* **2019**, *234*, 1857–1866. [CrossRef]
9. Wen, Z.P.; Wu, J.W.; Tan, J.B. An adaptive modeling method for multi-throttle aerostatic thrust bearing. *Tribol. Int.* **2020**, *149*, 105830. [CrossRef]
10. Zhou, Y.J.; Chen, X.D.; Chen, H. A hybrid approach to the numerical solution of air flow field in aerostatic thrust bearings. *Tribol. Int.* **2016**, *102*, 444–453. [CrossRef]
11. Kawai, T.; Ebihara, K.; Takeuchi, Y. Improvement of Machining Accuracy of 5-Axis Control Ultraprecision Machining by Means of Laminarization and Mirror Surface Finishing. *CIRP Ann.* **2005**, *54*, 329–332. [CrossRef]
12. Yoshimura, T.; Hanafusa, T.; Kitagawa, T.; Hirayama, T.; Matsuoka, T.; Yabe, H. Clarifications of the mechanism of nano-fluctuation of aerostatic thrust bearing with surface restriction. *Tribol. Int.* **2012**, *48*, 29–34. [CrossRef]
13. Chen, X.D.; He, X.M. The effect of the recess shape on performance analysis of the gas-lubricated bearing in optical lithography. *Tribol. Int.* **2006**, *39*, 1336–1341. [CrossRef]
14. Li, Y.F.; Yin, Y.H.; Yang, H.; En, L.X.; Mo, J.; Cui, H.L. Modeling for optimization of circular flat pad aerostatic bearing with a single central orifice-type restrictor based on CFD simulation. *Tribol. Int.* **2017**, *109*, 206–216.
15. Zhu, J.C.; Chen, H.; Chen, X.D. Large eddy simulation of vortex shedding and pressure fluctuation in aerostatic bearings. *J. Fluid Struct.* **2013**, *40*, 42–51. [CrossRef]
16. Aoyama, T.; Kakinuma, Y.; Kobayashi, Y. Numerical and Experimental Analysis for the Small Vibration of Aerostatic Guideways. *CIRP Ann.* **2006**, *55*, 419–422. [CrossRef]
17. Gao, S.Y.; Cheng, K.; Chen, S.J.; Ding, H.; Fu, H.Y. CFD based investigation on influence of orifice chamber shapes for the design of aerostatic thrust bearings at ultra-high speed spindles. *Tribol. Int.* **2015**, *92*, 211–221. [CrossRef]
18. Chen, X.D.; Chen, H.; Zhu, J.C.; Jiang, W. Vortex suppression and nano-vibration reduction of aerostatic bearings by arrayed microhole restrictors. *J. Vib. Control* **2016**, *23*, 842–852. [CrossRef]

19. Feng, K.; Wang, P.; Zhang, Y.J.; Hou, W.J.; Li, W.J.; Wang, J.W.; Cui, H.L. Novel 3-D printed aerostatic bearings for the improvement of stability: Theoretical predictions and experimental measurements. *Tribol. Int.* **2021**, *163*, 107149. [CrossRef]
20. Lentini, L.; Moradi, M.; Colombo, F. A Historical Review of Gas Lubrication: From Reynolds to Active Compensations. *Tribol. Ind.* **2018**, *40*, 165–182. [CrossRef]
21. Eleshaky, M.E. CFD investigation of pressure depressions in aerostatic circular thrust bearings. *Tribol. Int.* **2009**, *42*, 1108–1117. [CrossRef]
22. Gao, W.; Arai, Y.; Shibuya, A.; Kiyono, S.; Park, C.H. Measurement of multi-degree-of-freedom error motions of a precision linear air-bearing stage. *Precis. Eng.* **2006**, *30*, 96–103. [CrossRef]
23. Li, L.Q.; Lou, J.L.; Nishikawa, H.; Luo, H. Reconstructed discontinuous Galerkin methods for compressible flows based on a new hyperbolic Navier-Stokes system. *J. Comput. Phys.* **2021**, *427*, 110058. [CrossRef]
24. Li, L.Q.; Lou, J.L.; Luo, H.; Nishikawa, H. High-Order Hyperbolic Navier-Stokes Reconstructed Discontinuous Galerkin Method. In Proceedings of the AIAA Scitech 2019 Forum, Dallas, TX, USA, 17–21 June 2019.
25. Kabir, H.; Aghdam, M.M. A robust Bézier based solution for nonlinear vibration and post-buckling of random checkerboard graphene nano-platelets reinforced composite beams. *Compos. Struct.* **2019**, *212*, 184–198. [CrossRef]
26. Kabir, H.; Aghdam, M.M. A generalized 2D Bézier-based solution for stress analysis of notched epoxy resin plates reinforced with graphene nanoplatelets. *Thin Wall Struct.* **2021**, *169*, 108484. [CrossRef]
27. Li, Y.T.; Zhao, J.Y.; Zhu, H.X.; Lin, Y.X. Numerical analysis and experimental study on the microvibration of an aerostatic thrust bearing with a pocketed orifice-type restrictor. *Proc. Inst. Mech. Eng. J. Eng. Tribol.* **2014**, *229*, 609–623. [CrossRef]
28. Nicoud, F.; Ducros, F. Subgrid-scale stress modeling based on the square of the velocity gradient tensor. *Flow Turbul. Combust.* **2002**, *34*, 349–374.
29. Piomelli, U.; Balaras, E. Wall-layer models for large-eddy simulations. *Ann. Rev. Fluid Mech.* **2002**, *34*, 349–374. [CrossRef]
30. Zhu, J.C.; Chen, H.; Chen, X.D. Numerical Simulation of the Turbulent Flow in Ultra-Precision Aerostatic Bearings. *Adv. Mat. Res.* **2013**, *680*, 417–421. [CrossRef]